Nonmetric Camera Calibration for Underwater Laser Scanning System

Chau-Chang Wang, *Member, IEEE*, and Min-Shine Cheng

Abstract—This paper describes the development of an underwater camera system with a laser line source to measure seafloor features at millimeter scales. The quality of underwater photography is limited by the visibility of the water column. In real underwater environments, there are always suspended particles in the water column and light is scattered by these particles. As a result, photographic images taken under such conditions will be blurred. The stronger the light source is, the more severe the blurring will be. Therefore, it is difficult to discern the features of the intended target directly from the underwater images. To overcome this problem, a laser stripe can be projected onto the target and the profile of the target can be inferred from the displacement of the laser scan lines relative to a reference baseline. With a calibrated camera, the displacement expressed in pixels can be converted into the dimensions of the target in engineering units. To obtain a broader view in a closer distance, a wide-angle lens is usually used. As a result, the image taken with the wide-angle lens is nonlinear and is strongly distorted at the edges of the image. Calibration of a camera involves finding the optical and geometrical parameters of the camera and the environment in which it works. In this paper, a modified coordinate mapping calibration procedure is used. We divide the scope of the camera into several regions and build linear mappings between the world coordinate system and the pixels in the regions. We lay vertical and horizontal grid lines separated by 50 mm on an acrylic board that is aligned with the laser scanning sheet. These grid lines serve as longitude and latitude lines of a map. On the captured image, we curve-fit the grid points in pixel coordinates. A pair of interpolated longitude and latitude lines which pass through the target point are used to estimate the location of the point in the world coordinate system. We assess the accuracy of this procedure with test pieces (grooved blocks and seabed ripples) fabricated by a computer numerical control milling machine. Our measurements show that the error is less than 1.5 mm when the target is scanned from a distance of 1 m.

Index Terms—Charge-coupled devices (CCDs) calibration, laser scan, seabed roughness.

I. INTRODUCTION

THE surface of a seabed is affected by wave motions, current disturbance, sediment transportation, and biological activities. The scale of the features on the seabed varies from

C.-C. Wang is with the Institute of Undersea Technology and Asian Pacific Ocean Research Center, National Sun Yat-sen University, Kao-Hsiung 804, Taiwan (e-mail: chauwang@mail.nsysu.edu.tw).

M.-S. Cheng was with the Institute of Undersea Technology, National Sun Yat-sen University, Kao-Hsiung 804, Taiwan. He is now with ProMOS Technologies, Hsinchu 30078, Taiwan.
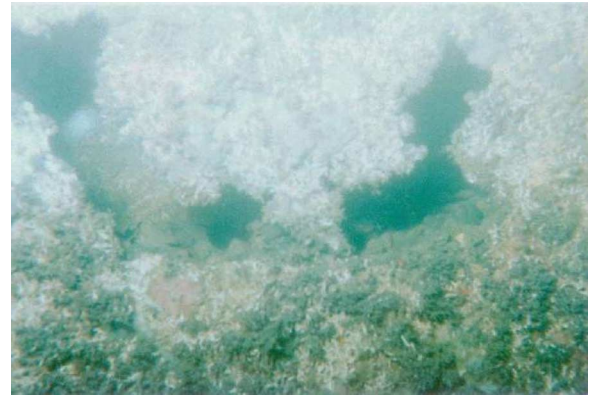
Fig. 1. Sample underwater photograph taken during a pier inspection.

meters for large sandwaves to less than 1 mm for prints left by biological activities. The roughness of the seabed is one of the key parameters in modeling high-frequency underwater acoustic wave scattering. Marine biologists are also interested in the evolution of prints on a seabed because it reveals the quantity and activity of benthos. In this paper, we present the design and calibration scheme of an underwater laser scanning system which is capable of measuring seabed features with millimeter resolution.

Photography is frequently used as a monitoring or surveying tool for underwater research. It can provide qualitative information for archaeological site documentation and coral reef habitat monitoring [1], [2]. However, unlike its counterpart in the air, underwater image quality is strictly limited by illumination, range, and environmental factors such as turbidity. If the target is several meters away from the camera, even under the best water conditions, photographs cannot give satisfactory results. For example, Fig. 1 is a photograph taken during an underwater safety inspection of pier structures. The gray area is a patch of barnacle settlement and the dark area is a rust pot. Unless we know what we are looking at in the photograph, the undersea world usually lacks reference objects to assist in determining the nature or the dimension of features. To extract quantitative information from photographs, an approach widely adopted in aerial image interpretation is *stereovision*. The working principle is illustrated in Fig. 2. First, a pair of conjugate images taken from two known perspectives is compared [3]. Pixels that belong to the target point are matched or *registered* on both images. In this model, the target point, focal point, and registered pixel point are assumed to be collinear, so rays L_L and L_R can be used to calculate the location of the target point in the object space [4], [5]. The cameras and the environment are characterized by two groups of parameters: the intrinsic
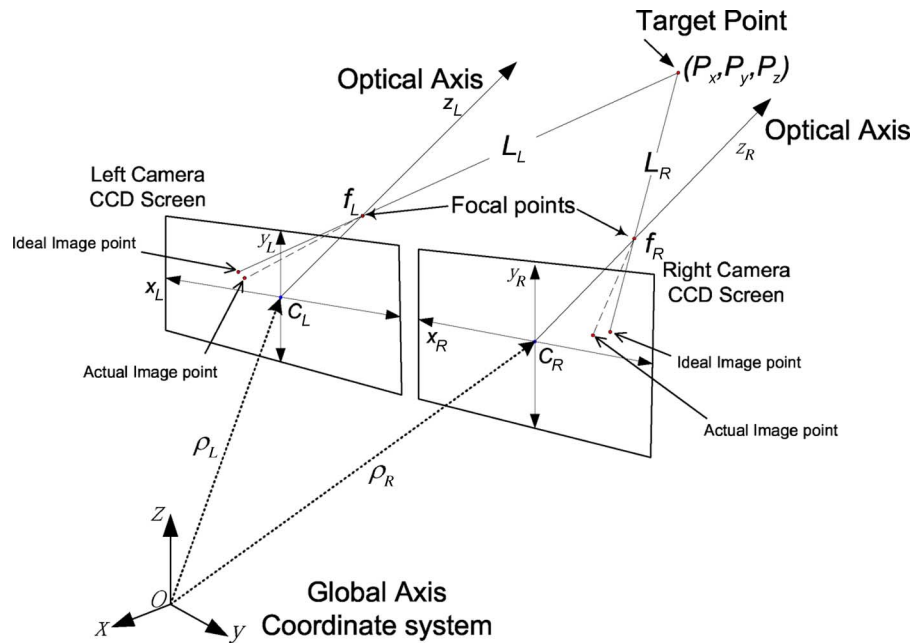
Fig. 2. Principle of stereophotography and the parameters used in the pinhole model.

and extrinsic parameters. As shown in Fig. 2, the former includes focal length, optical distortion, and nonlinearity of the charge-coupled device (CCD) screen; the latter consists of the location and orientation of the camera described in the world coordinate system. All together, 11 or more parameters are adopted in modeling for various algorithms [6]. The more parameters are included, the more accurate the geometric and optical models can be. However, this comes with the price of computation complexity. No matter how many parameters are used in the model, this type of calibration involves solving a system of nonlinear equations or performing a nonlinear optimization process. Many researchers have proposed various methods to achieve faster or more convenient calibration for CCD cameras but most of them are restricted to use in the air because the refraction between water and glass can cause a large distortion which is not included in the model.

For underwater applications, the photogrammetric model becomes more complicated because the refraction effects between the air/viewport-glass interface and the viewport-glass/water interface invalidate the triangulation collinearity assumption. Li *et al.* took refraction indices into account and revised the model of the underwater camera system as a 3-D optical ray tracing problem [7]. They proposed to calibrate the camera with two independent phases. In phase one, the cameras are calibrated with conventional techniques in the air without the viewport glass to obtain all model parameters but the refraction-related ones. In the second phase, the viewport glass is sealed with the camera housing, and a two-stage refracted ray tracing model is used to determine parameters associated with the viewport glass, such as the viewport glass's center and curvature. In this stage, a 3-D rigid frame with known positions is submerged in the water to provide images for calibration. The refraction indices of water and glass are assumed to be known and fixed to simplify the computation. However, in field applications, these parameters are a function of temperature and pressure; and the rigidity of the

calibration frame is always less than ideal. To overcome these problems, Harvey and Shortis adopted a method called the *free network solution* which models implicitly the viewport geometry and the refraction indices in the calibration parameters [8]. To assess the quality and stability of the calibration, they performed a series of experiments to quantify the variations of the camera model parameters in terms of error magnitude and significance. They came to a conclusion that the stereovideo system remains stable in the controlled environment. However, there are significant changes to some of the parameters if the system is disassembled for transport between sites or for access to the recorded tapes.

The stereovision technique does not need an auxiliary light source and is classified as *passive vision*. It works well unless the photographs have only smoothly textured areas, repetitive structures, or unclear images. In these cases, registration of target features is hard to achieve. To overcome this limitation and increase the image signal-to-noise ratio (SNR), another simple technique used in machine vision is to project structured light onto the scene and infer detailed information of various features from the distortion of the structured light in the image [9]–[11]. Active light sources are used, so it is classified as *active vision*. One of the structured light patterns commonly used is a light stripe generated by placing a cylindrical lens or a narrow slit in front of a laser source, as shown in Fig. 3. We can see that the light stripe projected on the target blocks leaves a trace on the surface. This trace is the cross section of the block at that location. A CCD camera can be placed at a proper distance with an oblique perspective angle to observe the deformed light stripe. The laser stripe seen in the CCD camera is similar to the silhouette of the target (as shown in Fig. 4). The high contrast of the laser scan line in the image can be extracted by proper thresholding. It should be noted that the offset of the laser line is not necessarily proportional to the height of the target because the camera is pointed at an oblique angle to the target such that the
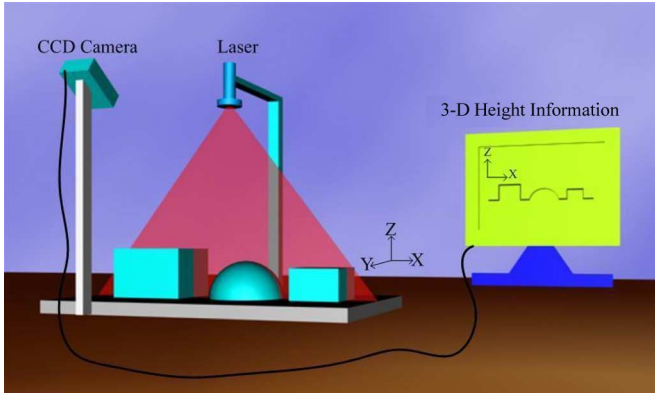
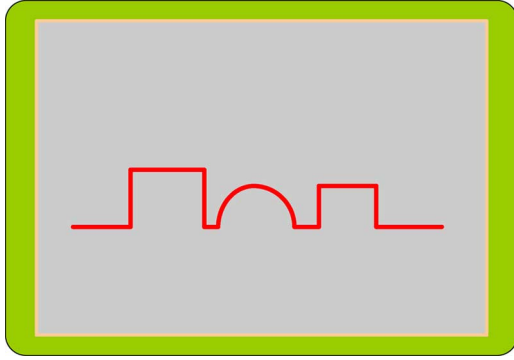Fig. 3. Laser light stripe projected on a target.

Fig. 4. Distorted laser line seen from the CCD camera in Fig. 3. From left to right, the laser line departs from the baseline in a fashion similar to the profile of the target.

image generally has some distortion. Therefore, a calibration is necessary to convert the laser scan line described in pixel coordinates into the actual dimension of the profile [12]. Applying this idea in the water, the Harbor Branch Oceanographic Institution, Ft. Pierce, FL, installed a laser line scanning system in their Johnson-Sea-Link submersible to locate possible seafloor rock outcrops [13], [14]. Crawford and Hay constructed a laser scanning system to record the seabed elevation variation and suspension events [15]. Their system is capable of providing a 2-D structure of the suspended sediment field with millimeter-resolution ripple elevation measurement over a range of 1 m. To have a full 3-D measurement of the environment, the scanning head needs to be mounted on a linear track or rotating shaft to provide a third degree of freedom. As a result, for such a line scanning system, full 3-D modeling of the camera is not necessary. The camera calibration can be simplified as finding a 2-D-to-2-D mapping, i.e., points in pixel coordinates to coordinates on the laser scanning plane. Chen and Kak took this idea and simplified the optical model [16]. They used a 4×3 transformation matrix to characterize this mapping. Theoretically, only four object points at known locations are required to determine this matrix. This method is attractive because it does not involve any low-level details of the camera and the projection light model parameters. On the other hand, because the transformation matrix is constant over the entire image, the nonlinearity of the optics of the camera cannot be counted for in the entire field of view. Instead of this simplified linear mapping

matrix, another approach is to use multiple regression for relating a group of grid points on the laser scanning plane to their images in the pixel coordinates [17]. For example, in Fig. 5, we show schematically a grid with known spacing and the corresponding image captured by a CCD camera. Assume that for all feature points (intersections of grid lines), the locations in the scanning plane coordinate system (S_k, R_k) and the pixel coordinate system (u_k, v_k) are available. We can construct two multivariable polynomial functions to relate the two coordinate systems

$$S_k \approx S'_k(u_k, v_k) = \sum_{j=0}^{j=N} \sum_{i=0}^{N-j} C_{ij} u_k^i v_k^j$$

$$R_k \approx R'_k(u_k, v_k) = \sum_{j=0}^{j=N} \sum_{i=0}^{N-j} D_{ij} u_k^i v_k^j \tag{1}$$

where N is the order of regression and C_{ij} and D_{ij} are the regression coefficients to be determined. For m feature points, we define error functions E_S and E_R as

$$E_S = \sum_{k=1}^{m} (S'_k - S_k)^2$$

$$E_R = \sum_{k=1}^{m} (R'_k - R_k)^2.$$

Thus, the regression coefficients can be found by solving the following:

$$\frac{\partial E_R}{\partial C_{ij}} = 0$$

$$\frac{\partial E_S}{\partial D_{ij}} = 0. \tag{2}$$

This approach is simple; however, for uneven distorted images, it is difficult to find appropriate polynomial functions to accurately characterize the nonlinearity.

A tradeoff between accuracy and computational complexity is necessary for a feasible calibration method. Furthermore, the calibration method also needs to be simple enough to perform in water. Some calibration schemes require the manipulation of a control frame that is assumed to be rigid in the water [18]. This condition will be difficult to fulfill if the sea state is not calm. In this paper, we do not view the calibration as a problem of finding intrinsic and extrinsic parameters for the camera model, but instead as an empirical method in which the view seen by the CCD camera is split into smaller regions and local linear maps are built for each region. Ideas analogous to longitude and latitude lines of a map are adopted to refine the accuracy of laser line scanning. We utilize the properties of the structured-light-oriented geometry to simplify the process, while the desired accuracy is maintained. The system is intended to measure underwater features with millimeter resolution in general. However, in this paper, we focus on its application to acquire seabed roughness, one of the key parameters in modeling high-frequency underwater acoustic wave scattering. In this paper, 1) a map projection geometry is introduced to derive a computationally efficient algorithm for calibrating CCD cameras used for structural light scanning, 2) a step-by-step analysis of
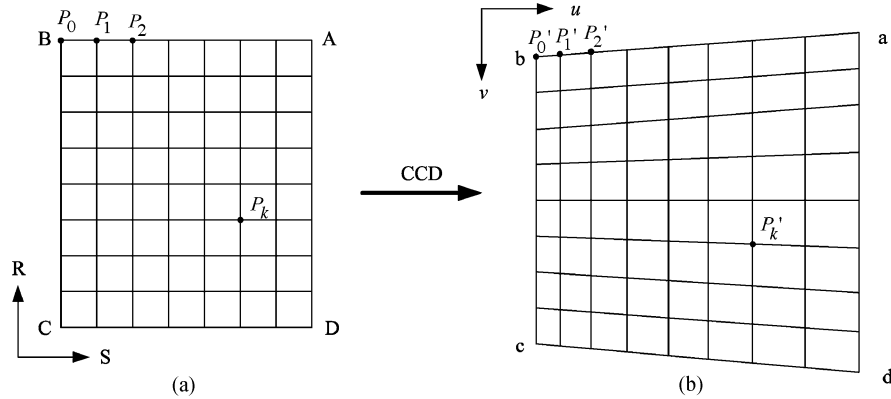
Fig. 5. (a) Schematic drawing of a calibration grid and (b) its image seen in a CCD camera.

the measurement error bounds is presented, 3) precise point-to-point comparisons between test pieces fabricated by a computer numerical control (CNC) milling machine and the scanning data are provided to verify the efficacy of our approach, and 4) a ripple seabed model is scanned and data of different slices are analyzed to demonstrate the performance of the system at a surface level as opposed to a point level. The design of this seabed model is meant to serve as a ground truth to evaluate the performance of the scanning system. The resolution and accuracy set the limits of the roughness of the seabed which the system can measure in the field and restricts the frequency range for acoustic applications. However, in this paper, we will only focus on the issues related to geometry.

The structure of the rest of the paper is as follows. In Section II, the ideas of our calibration process are explained. We outline the computational procedures in Section III. Several experiments and the performance of this approach are reported in Section IV. We discuss some of the potential error sources and the possible remedies in Section V. Finally, we conclude this paper with Section VI.

II. CALIBRATION SCHEME

Before explaining the calibration method, let us first review the concept of map projection. Consider a transparent hemisphere with longitude and latitude lines on its surface as shown in Fig. 6. To make a map of this region, we need to unwrap the hemisphere into a flat 2-D plane. However, the hemisphere is topologically incompatible with a sheet of flat paper and we will have a map which is either torn or distorted. For an untorn but distorted map, we may put a light source at the top of the hemisphere and a screen tangent to the south pole. The terrain and the longitude and the latitude lines projected on the screen create the map. The longitude and the latitude lines provide correspondence between where we are looking on the map and its actual location on the hemisphere. For a location that is not right on a longitude or a latitude line, we estimate its coordinates from the ratio of the distances to the neighboring longitude/latitude lines. For this type of projection, the area around the south pole is less distorted than the area close to the equator on the map. Given the geometry of the globe, the location of the light source and the projection screen, we can produce such a map analytically with projective geometry. Bearing this idea in mind, the
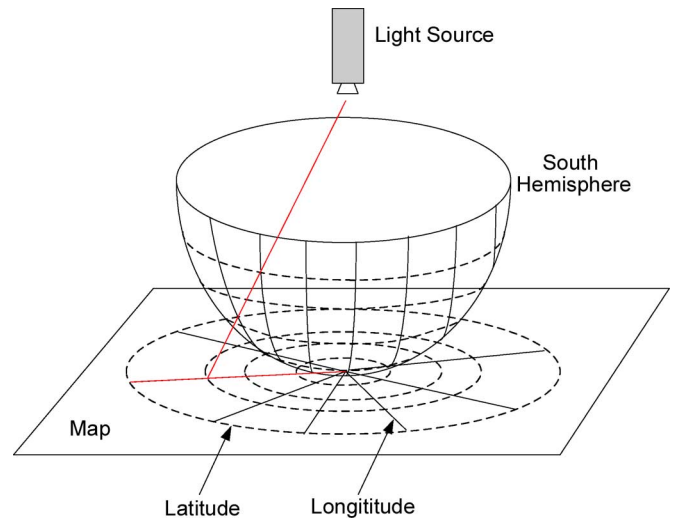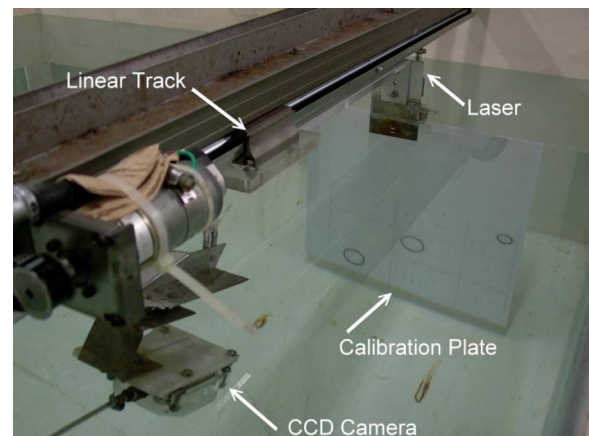

Fig. 6. Map projection.

Fig. 7. Experimental setup.

CCD camera calibration for laser line scanning is an analog of the projection problem if we treat the CCD as the projection screen and a board printed with known longitude and latitude lines pattern placed coplanarly with the laser scanning sheet replacing the transparent hemisphere. The setup shown in Fig. 7 demonstrates this arrangement.
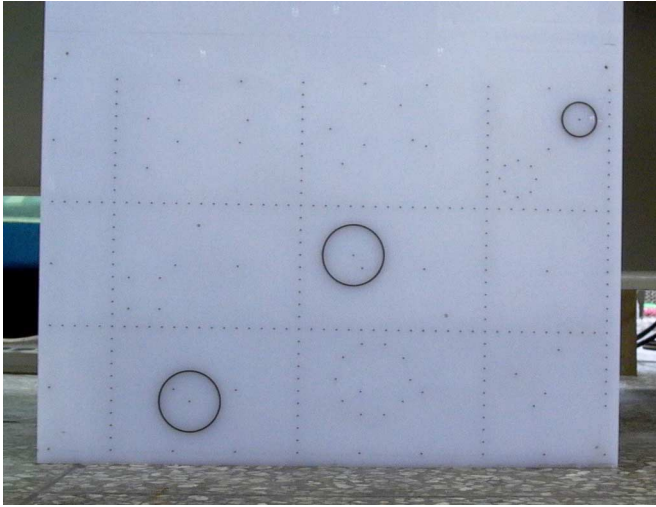
Fig. 8. Calibration board with vertical and horizontal grid points drilled by a CNC machine.
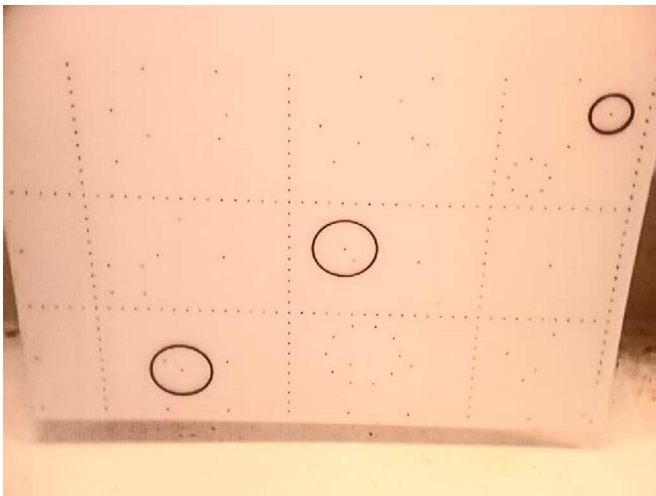

Fig. 10. Longitude and latitude lines created by curve-fitting the grid dots.

Fig. 9. Calibration board seen from the CCD camera.

Fig. 11. Closeup of a target point T on the calibration board.

For our calibration setup, we lay grid points on an acrylic board as shown in Fig. 8. These grid points are drilled with 50-mm separation by a CNC milling machine. This board, called the *calibration board* hereafter, is carefully aligned with the plane of the laser scanning sheet. To cover a larger view, a wide-angle CCD camera is placed roughly 1 m away from the board. The axis of the CCD camera is pointed downward approximately 30° from the horizon. The points seen in the CCD camera are shown in Fig. 9. It is obvious that the image in the upper half is larger than in the lower half of the frame and the points are no longer along straight and parallel lines but are curvilinear near the boundary of the image frame. However, this distortion is mild and changes smoothly from the center to the sides. If we curve-fit the grid points to create longitude lines V_j and latitude lines H_i, as shown in Fig. 10, the scope of the CCD camera is divided into smaller quadrangular regions. Within a quadrangle, we can assume that the distortion of the image is smooth and linear. Therefore, given a target point
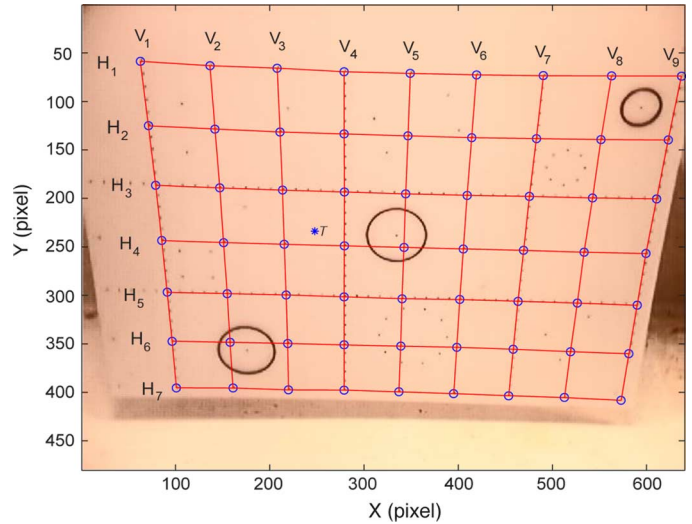
T, shown in Fig. 10, or the closeup in Fig. 11, its location on the calibration board can be estimated from the distances (in pixels) between itself, V_j, V_{j+1}, H_i, and H_{i+1}. A rough estimate of T is approximately one half of a span from V_j and three quarters of a span from H_i. In other words, its location is roughly 25 mm right from the longitude line V_j and 37.5 mm beneath the latitude line H_i. Since the grid points were laid with 50-mm spacing, the coordinates of T can be inferred from the closest known point, e.g., R. For example, if R's coordinates are (100 mm, 250 mm) in the calibration board coordinate system, T will be around (125 mm, 212.5 mm).

In the measurement, we calculate the position of the target point with respect to a corner of the quadrangle. The idea is to interpolate from the surrounding longitude and latitude lines a set of vertical and horizontal lines which intersect at the target
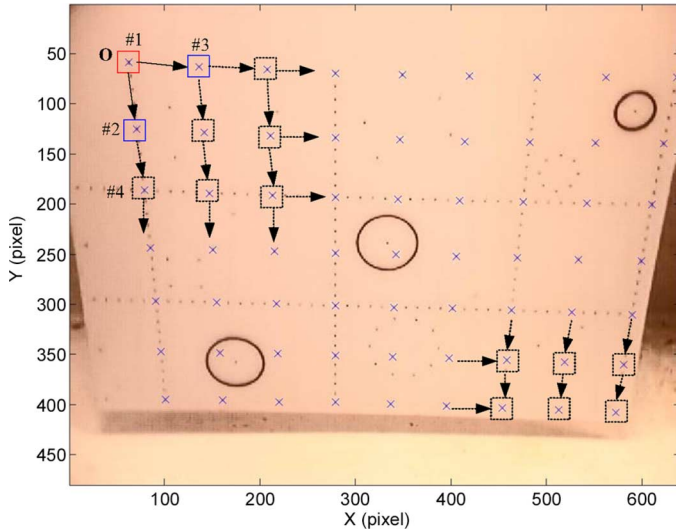
Fig. 12.   Idea of adaptive searching for control points on the calibration board.

point.[1] For the example point T, we can combine H_i and H_{i+1} together to have a horizontal line H which passes through T as

$$H = w_i H_i + w_{i+1} H_{i+1} \qquad (3)$$

where $w_i, w_{i+1} \geq 0$, and $w_i + w_{i+1} = 1$. If the weighting factors ratio is $w_i/w_{i+1} = 0.26/0.74$, we find that T is 50 mm $\times$ 0.74 = 37 mm beneath H_i, or 50 mm $\times$ 0.26 = 13 mm above H_{i+1}. The horizontal component can be obtained similarly.

This method does not explicitly involve any intrinsic or extrinsic parameters of the CCD camera or the relative position of the laser scanning sheet. All nonlinearities are lumped together and linearized separately for each quadrangle in the map. Therefore, when a laser scanning sheet is projected on the target, the relative position of the laser line segment in the calibration board coordinate system can be calculated with the same idea. In Section III, we will present the procedures of constructing such a projection map for the laser scanning system.

III. IMPLEMENTATION

First of all, we define the following terms used in explaining the calibration and measurement procedures.

1) *Control points*. Grid dots with 50 mm separation, called control points, are laid on the surface of an acrylic board as shown in Fig. 8. We create these dots with a CNC milling machine, so their positions are assumed to be accurate to the CNC machine accuracy which is 0.01 mm for our case. Each dot is of finite size and we use its center to represent the position of the point. As shown in Fig. 12, the distances between control points in the CCD image are not fixed but varying smoothly from point to point. An algorithm was developed to search for the control points adaptively. As a first step, we manually select the upper-left dot (bounded in box #1), the dot beneath (bounded in box #2), and right next to it (bounded in box #3). We use the displacement

---

[1]With the functional forms of the neighboring longitude and latitude lines, we can use bisection to decide a set of vertical and horizontal lines which intersect at the target point.

vector from dots #1 to #2 as a reference to estimate the approximate location of the control point beneath #2 (denoted as #4). A bounding box is placed at the tip of the displacement vector to search for the dot. Once dot #4 is found, a new displacement vector from #2 to #4 can be used to search downward further. In the same manner, we can search toward the right-hand side. This process is repeated until all the control points are located. The search pattern is shown in Fig. 12. The center of a dot (X, Y) in pixels is determined by fitting the region around the brightest pixel with a second-order polynomial and using the maximum as the center [19]. We mark all the control points found with an "$\times$" as shown in Fig. 12. The control point at the upper-left corner labeled as "O" is selected as the origin of the calibration board coordinate system.

2) *Longitude and latitude lines*. All the control points are laid with equal spacing on the board. Therefore, the trend of the local image distortion is characterized by the relative displacement of the control points and the overall distortion can be characterized by the vertical (longitudinal) and horizontal (latitudinal) lines which are obtained by curve-fitting the control points (in pixel coordinates). To achieve better fitting results, the latitude lines are described as $Y = Y(X)$, while the longitude lines are described as $X = X(Y)$. In Fig. 13, we show the image of horizontal control points overlaid with curves obtained by three different fitting functions. From top to bottom, they are first-order root-mean-square (rms), second-order rms, and cubic B-spline. In the case of first-order rms, the straight line can only pass through the neighborhood of control points, not right through them. As for second-order rms, the polynomial curve does not pass through the control points either, but it traces the control points closely. Mathematically, cubic B-spline curve is forced to pass all the control points. Because these longitude and latitude lines are used as bases to determine the location of a target point, the correctness of the curve fit for the control points strongly influences the accuracy of the measurement. We discuss the performance of these three fitting methods in Section IV.

3) *Reference marks and auxiliary rulers*. The longitude and latitude lines give us a rough idea of the location of a target point. The overall accuracy of the system could be improved by adding more control points on the calibration board to lay denser longitude and latitude lines. However, doing so would give us a crowded and confusing image and also increase the computational complexity. Alternatively, we can improve the accuracy by placing marks of smaller spacing at selective locations for reference. For example, in Fig. 14, we place reference marks of 10-mm spacing on the calibration board labeled as R_1 to R_5. We give these longitude and latitude lines another name, the *auxiliary rulers*. By the name *ruler* we mean that these reference lines help us to estimate where the actual coordinates are in a more accurate manner because the uncertainty is reduced from 50 to 10 mm.

We show again the closeup of T in Fig. 15. The interpolated latitude line H intersects with the closest vertical auxiliary ruler R_4 at T_4. T and T_4 are on the same latitude line, so they share the
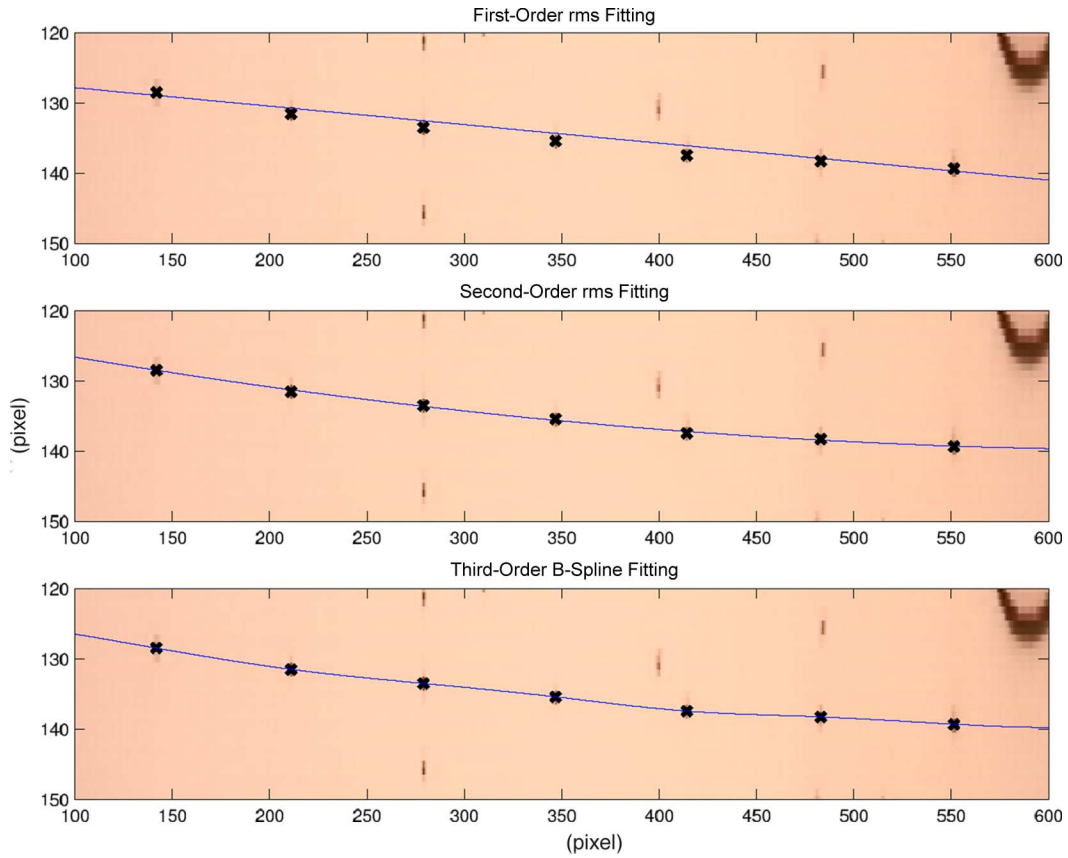
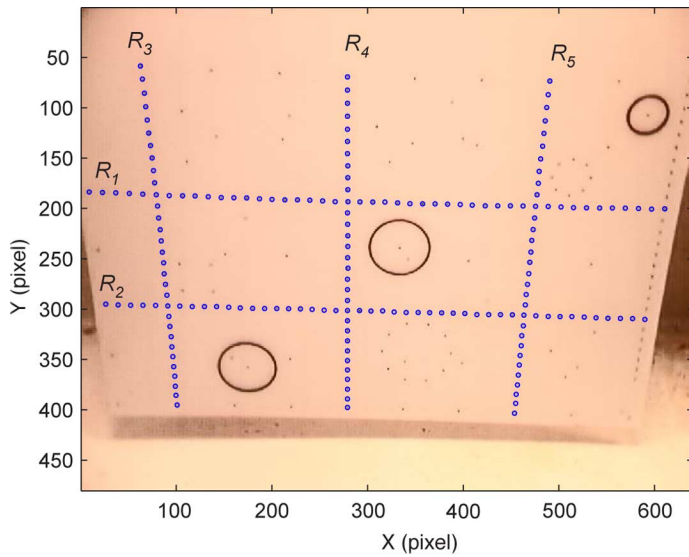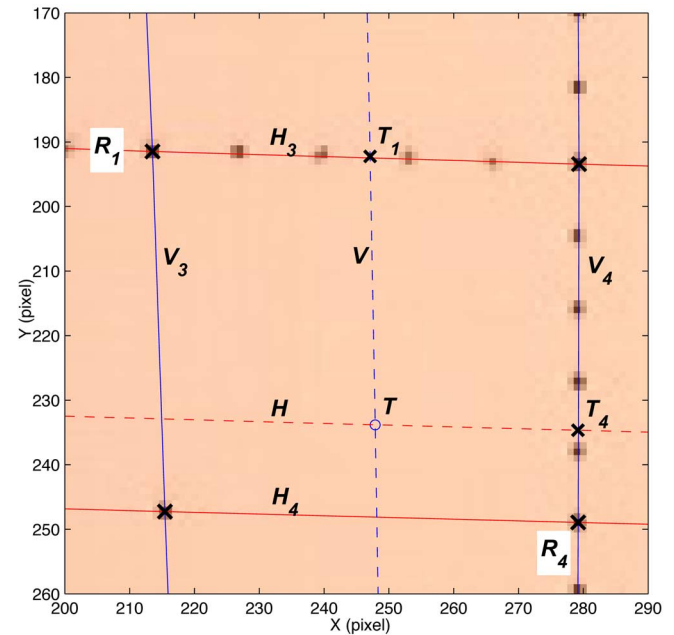Fig. 13.   Comparison of different fitting methods for grid points.

Fig. 14.   Five auxiliary rulers on the calibration board.

Fig. 15.   Closeup of a target point T on the calibration board.

same y coordinate. T_4's y coordinate can be obtained by interpolating between the two closest bounding reference marks on R_4. In Fig. 16, we plot the vertical pixel coordinate Y of each reference mark on R_4 versus the corresponding vertical coordinate y on the calibration board in millimeter. With this plot, the vertical component of T_4 in pixels is then used to look up its corresponding vertical coordinate in millimeter in the laser

scanning plane. For example, according to Fig. 16, T_4's Y is 234.5 pixels which is converted to 142.3 mm. It should be noted that because the auxiliary rulers are placed evenly on the calibration board, we should use the closest one for reference to have a better result. Likewise, T_1, the intersection of V with the
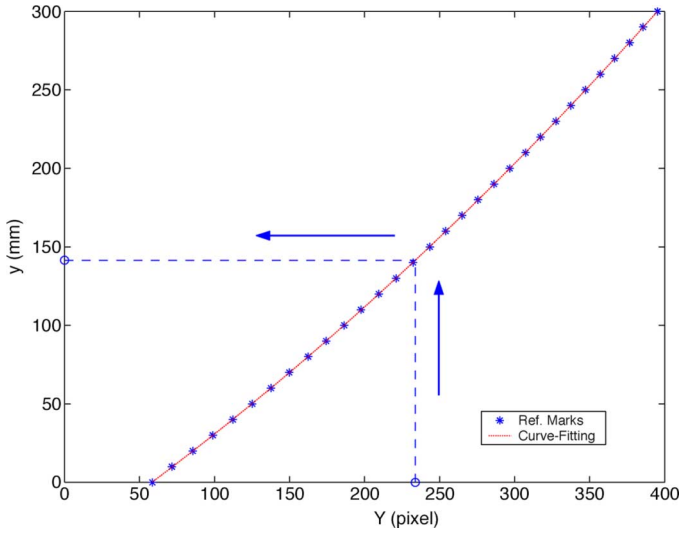
Fig. 16. Pixel coordinate of reference marks versus their calibration board coordinate for ruler R_4.
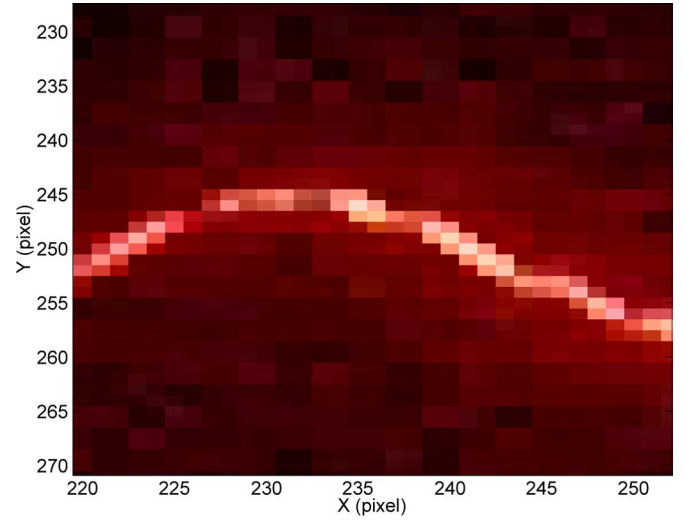

Fig. 17. Closeup image of a laser scan line casting on a sand ripple. It is obvious that the width of the laser line is more than one pixel.

nearby horizontal auxiliary ruler R_1, provides the x coordinate of T in millimeter.

We summarize the procedures as the following steps.

1) Choose two longitude lines and two latitude lines which surround the target point.
2) Iterate the weights (between one and zero) of the latitude lines until an interpolated curve passes through the target point.
3) Find the intersection of the interpolated latitude line with the closest vertical auxiliary ruler.
4) Substitute the vertical component of the coordinates found in step 3) into the ruler conversion curve to obtain the calibrated vertical coordinate of the point.
5) Repeat steps 2)–4) for the horizontal component.

The conversion of vertical and horizontal components are independent of each other, so they can be carried out simultaneously.

IV. EXPERIMENTS

The performance of the system depends on the accuracy of the longitude and latitude lines modeling and also the effectiveness of the laser scan line image processing. Ideally, we would like to have a laser scan line as narrow as possible (one pixel) in width.[2] In reality, the scan line is several pixels wide (see the bright area in Fig. 17). In other words, depending on how we choose the location of the center of the scan line, the result might be off by a couple of pixels. From the lookup curve shown in Fig. 16, we know that a pixel in the image frame is roughly equivalent to 1 mm in length on the calibration board. This ambiguity contributes to the error in the measurement. To understand the nature of these errors, it is necessary to carry out separate experiments to characterize the source and the contribution of the error types.

---

[2]One-pixel width also poses problems if we want to have subpixel resolution.
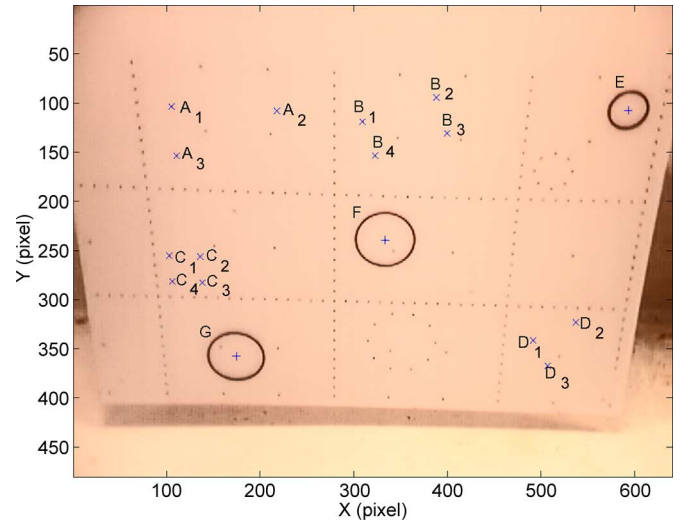

Fig. 18. Features on the calibration board for verification.

A. Onboard Verification

When making the calibration board, in addition to the control points and the auxiliary rulers, we also use the CNC milling machine to make several dots and shapes with known location and dimension. Measurement of the distance between two dots or the diameter of circles can be used to verify that the longitude and latitude lines curve-fitting achieves the required accuracy. Because three different functions are used to perform the curve-fitting, the performance of the different methods will be evaluated.

1) *Point-to-point distance*. There are several dots on the board, labeled as A_1–A_4, B_1–B_4, C_1–C_4, and D_1–D_4 in Fig. 18. We use the distance between points to estimate the error in our measurement. Because our approach is a point-based measurement, we expect to see that the absolute error remains bounded while the relative error tends to get smaller as the distance (denominator) increases. These results are summarized in Table I.

TABLE I
DISTANCE MEASUREMENT BETWEEN KNOWN POINTS. (THE NUMBER IN PARENTHESES IS THE NOMINAL DIMENSION GIVEN TO THE CNC MILLING MACHINE.)

Features Fitting Method	A_1A_2 (80.00 mm)			A_2A_3 (89.44 mm)			A_3A_1 (40.00 mm)		
	Measured	Err.	%	Measured	Err.	%	Measured	Err.	%
First rms	80.19	0.19	0.24	89.68	0.24	0.27	39.66	-0.34	-0.86
Second rms	80.01	0.01	0.01	89.43	-0.02	-0.02	39.84	-0.16	-0.39
Cubic B-Spline	86.82	5.82	7.28	94.73	5.28	5.91	40.10	0.10	0.26
Features Fitting Method	B_1B_2 (60.00 mm)			B_2B_3 (30.00 mm)			B_3B_4 (60.00 mm)		
	Measured	Err.	%	Measured	Err.	%	Measured	Err.	%
First rms	59.86	-0.14	-0.24	29.69	-0.31	-1.02	59.85	-0.15	-0.26
Second rms	59.80	-0.20	-0.33	29.90	-0.11	-0.35	59.84	-0.16	-0.27
Cubic B-Spline	63.77	3.77	6.28	30.03	0.03	0.09	63.89	3.89	6.48
Features Fitting Method	B_4B_1 (30.00 mm)			C_1C_2 (25.00 mm)			C_2C_3 (25.00 mm)		
	Measured	Err.	%	Measured	Err.	%	Measured	Err.	%
First rms	29.90	-0.10	-0.35	24.88	-0.12	-0.47	24.94	-0.06	-0.23
Second rms	29.88	-0.12	-0.39	24.91	-0.09	-0.37	25.09	0.09	0.35
Cubic B-Spline	30.16	0.16	0.55	25.62	0.62	2.49	25.09	0.09	0.37
Features Fitting Method	C_3C_4 (25.00 mm)			C_4C_1 (25.00 mm)			D_1D_2 (40.00 mm)		
	Measured	Err.	%	Measured	Err.	%	Measured	Err.	%
First rms	24.91	-0.09	-0.34	24.89	-0.11	-0.44	39.64	-0.36	-0.91
Second rms	24.91	-0.09	-0.34	24.95	-0.05	-0.20	39.82	-0.18	-0.46
Cubic B-Spline	25.58	0.58	2.33	24.90	-0.10	-0.42	40.45	0.45	1.13
Features Fitting Method	D_2D_3 (50.00 mm)			D_3D_1 (30.00 mm)					
	Measured	Err.	%	Measured	Err.	%			
First rms	49.66	-0.34	-0.68	30.45	0.45	1.51			
Second rms	49.72	-0.28	-0.57	30.11	0.11	0.38			
Cubic B-Spline	49.71	-0.29	-0.58	30.28	0.28	0.95			

2) *Diameter of circles.* Three circles, labeled as E, F, and G, are laid at the upper, middle, and lower part of the board. The circles are milled with a ϕ 0.8 end cutter and filled with the same black clay as used for control points. To obtain the diameter of the circle, we enlarge the image and manually pick out points on the circumference, as shown in Fig. 19. These points are used to best-fit a circle. The diameters obtained for the circles are listed in Table II. The results are accurate and are all well under 1% except for some measurements converted with cubic B-spline-fitted longitude/latitude lines.

Here, we define error as the measurement minus the nominal dimension, i.e., the value given to the CNC milling machine. Overall, first-order and second-order rms curve-fitting gives good measurement results. Almost all the relative errors of the measurement are less than 1% and the second-order result is better than that of first order. Surprisingly, the cubic B-spline curve-fitting does not perform well; its performance fluctuates. It ranges from 0.09% for $\overline{B_2B_3}$ to 7.28% for $\overline{A_1A_2}$. This poses problems for the scanning system because the error bound is
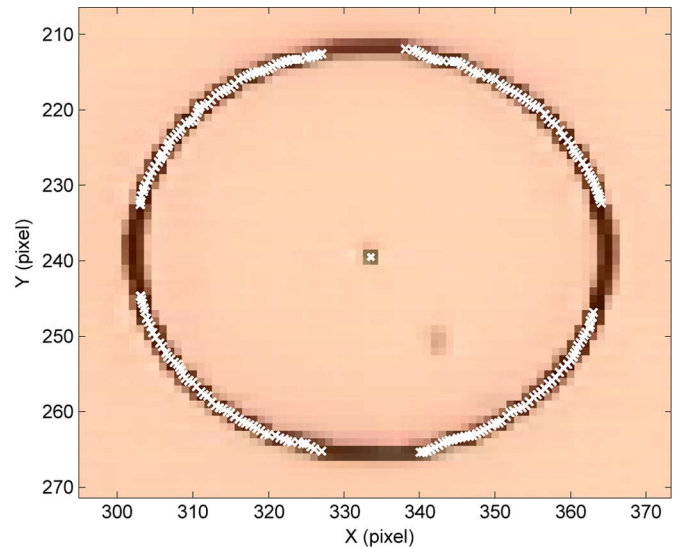

Fig. 19. Manually selected points (denoted as $\times$) on the circumference for estimating the diameter of circle E.

TABLE II
RESULTS OF ON-PLANE CIRCLES MEASUREMENTS. (THE NUMBER IN PARENTHESES IS THE NOMINAL DIAMETER OF THE CIRCLES.)

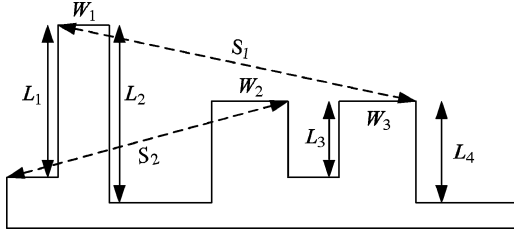| Features Fitting Method	E (28.40 mm)			F (49.20 mm)			G (49.20 mm)		
	Measure	Err.	Err. (%)	Measure	Err.	Err. (%)	Measure	Err.	Err. (%)
First rms	28.39	-0.01	-0.04	49.04	-0.16	-0.32	49.04	-0.16	-0.32
Second rms	28.22	-0.18	-0.64	49.09	-0.11	-0.22	49.07	-0.13	-0.26
Cubic Spline	29.17	0.77	2.70	50.39	1.19	2.42	49.63	0.43	0.88

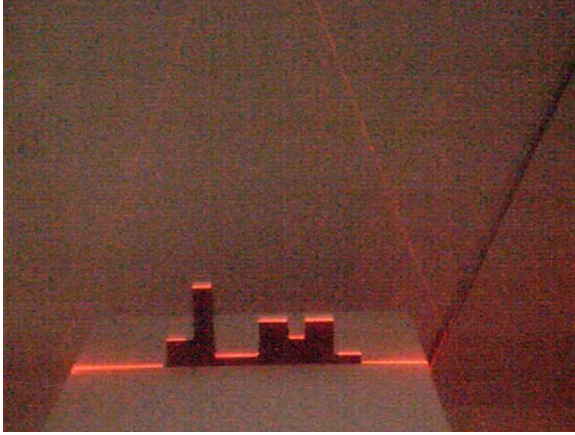Fig. 20. Dimensions of the grooved surface test piece.

Fig. 21. Snapshot of the grooved surface test piece scanning.

not stable. A discussion regarding this problem is presented in Section V. For the following experiments, we will only use second-order rms to fit the longitude/latitude lines.

B. Grooved Surface

The preceding experiments address the performance of the optical calibration alone. The final measurement result also depends on the properties of the laser line reflection from the target. For example a mirror-like surface may reflect the incoming beam perfectly. If the CCD camera is not pointing along the path of the reflection, it will not see the laser profile at all. Therefore, the texture of the target is a crucial factor. Also, we use a red-diode laser as light source, so if the color of the target is red or dark, the contrast is low and the SNR will be poor. To determine whether the calibration remains accurate for an actual surface, we use a CNC milling machine to make a test piece which has grooves of different widths and heights, as shown in Fig. 20. The laser profile seen from the CCD camera consists of line segments, as shown in Fig. 21. The discontinuity of the segment is the location where the height changes. We measure the widths, the heights, and the distances between edges and compare them with the

nominal dimension. For this experiment, the widths are defined by the end points of the laser segments. To determine the height, we cannot measure the distance between the edge of a top and the corner of a groove to be the height because the corner at the bottom of a groove is always a shadow zone where the laser cannot reach. Alternatively, we fit the points of the laser segment with a straight line and infer the height from the distance between the two lines. We find that the absolute errors, summarized in Table III, are all less than 0.6 mm. The measurement is accurate to 1% of the length of the features if the size is larger than 20 mm; so we may conclude that the calibration is effective.

C. Sandwave

One major goal is to use the system to measure the roughness of a sediment interface. To simulate the surface of a sandwave, we use a CNC milling machine to create a 3-D surface defined by

$$z(x, y) = (A + By)\sin(Cx + D\sin(Ey)) \qquad (4)$$

where x, y, and z are all in millimeters and A, B, C, D, and E are constants. There are two sine functions in this equation. The first one varies on the yz-plane that creates ripples while the other one, appearing in the argument of the first, undulates the ripples along the y-direction. The value of A determines the mean elevation of the surface, B determines how fast the amplitude of the ripple increases along the y-axis, C controls the wavelength of the ripples, and D and E define the undulating extent and frequency, respectively. The constants are chosen such that four ripples were accommodated in a $210 \times 210 \times 40$ mm^3 block.[3] The ripples meander and change direction twice in the model while the amplitude increases linearly along the y-direction from 1.5 to 8 mm. To simulate the granular texture of the seabed, we apply a thin layer of glue on the surface of the test piece and sprinkle it with sea sand. With this model, we can determine the lower limit of the amplitude which the system can detect. The computer-aided design (CAD) model and the workpiece is shown in Figs. 22 and 23, respectively.

A linear track carries the scanning head, moving in 0.5-mm increments, to profile the sandwave workpiece. Altogether, 400 images like the one shown in Fig. 24 are captured and processed to reconstruct the surface of the sandwave shown in Fig. 25. We plot all the data points and find that even the smallest amplitude (1.5 mm) of the sine wave is still visible on the plot. However, the waveform is tilted because the baseplane of the test piece is not necessarily aligned with the xy-plane of the scanning head. Therefore, with this misaligned data set, we can only have a qualitative description of the measurement.

[3]$A = 1.5$, $B = 0.043$, $C = 0.167$, $D = 2.0$, and $E = 0.042$.

| Features Fitting Method	W_1 (19.96 mm)			W_2 (29.96 mm)			W_3 (29.96 mm)		
	Measured	Err.	%	Measured	Err.	%	Measured	Err.	%
Second rms	20.03	0.07	0.34	29.76	-0.20	-0.67	30.12	0.16	0.53
Features Fitting Method	H_1 (60.00 mm)			H_2 (80.06 mm)			H_3 (20.04 mm)		
	Measured	Err.	%	Measured	Err.	%	Measured	Err.	%
Second rms	59.45	-0.55	-0.91	79.40	-0.66	-0.83	19.97	-0.07	-0.36
Features Fitting Method	H_4 (40.02 mm)			S_1 (154.96 mm)			S_2 (131.04 mm)		
	Measured	Err.	%	Measured	Err.	%	Measured	Err.	%
Second rms	39.67	-0.35	-0.89	154.56	-0.40	-0.26	130.73	-0.31	-0.24
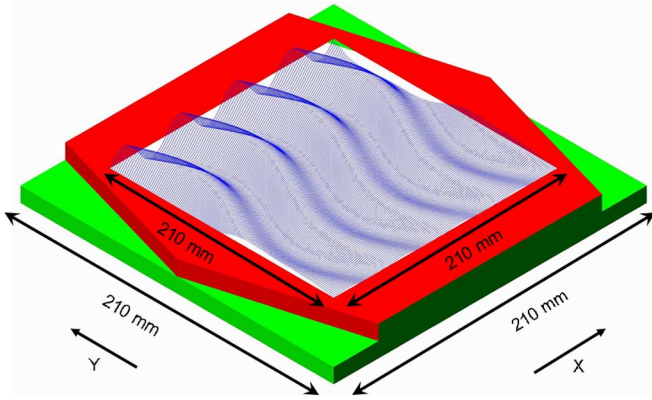
Fig. 22. CAD model of the sandwave surface.
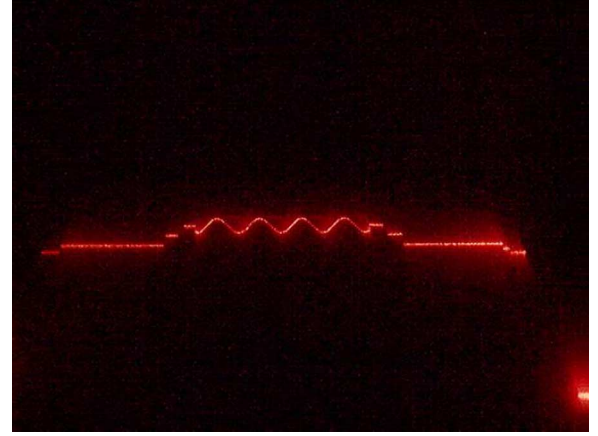
Fig. 24. Sample image of the sandwave scanning.

Fig. 23. CNC machined workpiece of the simulated sandwave.

Fig. 25. Raw data of the sandwave scanned.

To analyze the measurement quantitatively, for example comparing a slice of the measurement with the CAD model, we need to reorient and translate the measured surface such that a specific feature on the block and in the image is aligned. To achieve this, we added two wedges on both sides of the block along the y-direction. The top of the wedges is flat and is used as the baseplane for reference. First of all, we use points on the flat top of the wedges to best-fit a plane. The unit normal vector of this plane $\hat{n} = (n_x, n_y, n_z)$ is used to construct the following two rotational matrices about the x- and y-axes:

$$R_x = \begin{bmatrix} 1 & 0 & 0 \\ 0 & \sin\alpha & -\cos\alpha \\ 0 & \cos\alpha & \sin\alpha \end{bmatrix} \qquad (5)$$

$$R_y = \begin{bmatrix} \sin\beta & 0 & \cos\beta \\ 0 & 1 & 0 \\ -\cos\beta & 0 & \sin\beta \end{bmatrix} \qquad (6)$$
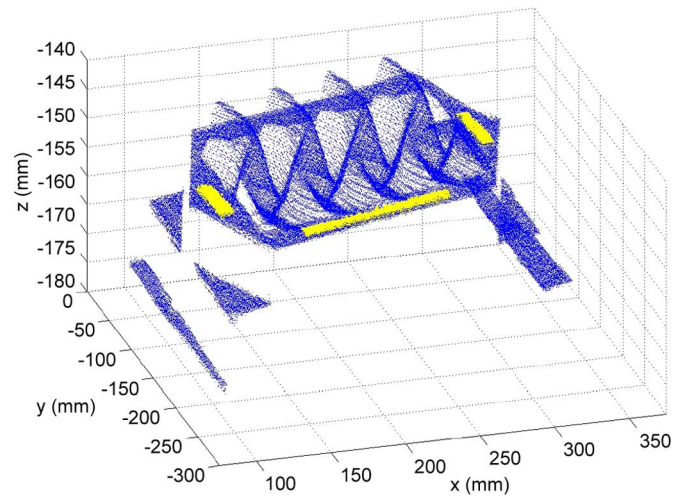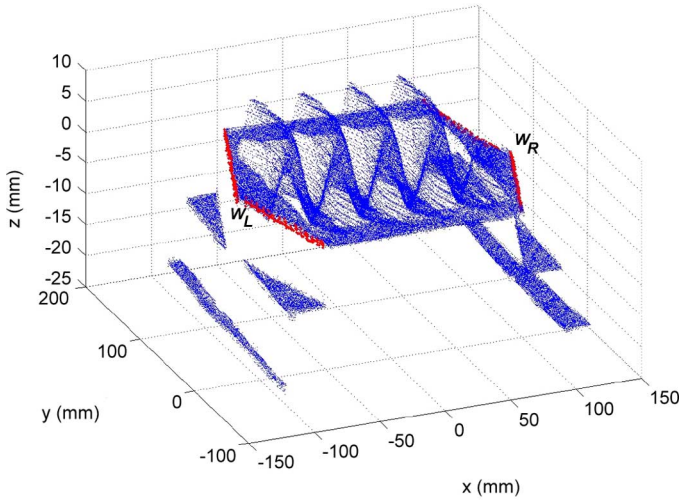
Fig. 26.   Sandwave surface after reorientation.

Fig. 27.   Contour plot of the sandwave surface (before yawing calibration).

where $\alpha = -\sin^{-1}(n_y)$ and $\beta = \sin^{-1}(n_x)$. All of the raw data P_{raw} are then subjected to the following two rotations to obtain the points P_{new} in the adjusted coordinate system:

$$P_{\text{new}} = R_x R_y P_{\text{raw}}. \tag{7}$$

After one round of adjustment, we recalculate the normal vector of the best-fit plane.[4] The procedure is repeated until $\hat{n}$ settles at (0, 0, 1). We plot the data points after reorientation in Fig. 26.

The next step is to rotate the block about the z-axis until the lower edge of the block lines up with the x-axis. This adjustment can be carried out by aligning the directional vector of the corners on the wedges, denoted as W_L and W_R in Fig. 26, with the x-axis. However, we cannot positively identify W_L and W_R from the data set because the laser line may not pass through them in the scanning process. An alternative is to infer their location indirectly from the intersection of the sides of the wedges. There is an abrupt change of height for the sides, so their corresponding data points can be extracted with a simple comparison of the elevation. These points are then used to determine the line corresponding to the edge. Theoretically, these two lines should meet at one point which is the corner of the wedge. In reality, the two lines would only get very close near the corner since the measurement cannot be perfect. These lines are projected onto the baseplane and the projected intersection is used to represent the corner of the wedge. The next step is to carry out a rotation about the z-axis such that the directional vector W_L to W_R is aligned with the x-axis. We show the contour of the surface after this rotation in Fig. 27.

It can be noticed immediately that the four sides form a parallelogram rather than a square. This distortion comes from the residual yawing angle between the laser scanning sheet and the linear track. For a single scan, the relative geometry of the profile is preserved, but there is a small shift along the cross-track direction between profiles. We need to calibrate this angle to

Fig. 28.   Contour plot of the sandwave surface (after yawing calibration).

restore the true shape of the test piece. Since the four sides of the workpiece are CNC-machined, the two sides along the y-direction should be orthogonal to the centerline $\overline{W_L W_R}$. With the line equations of the left side and the centerline $\overline{W_L W_R}$, we find that the yawing angle is 2.20° for this specific case; so we shifted all profiles in the negative x-direction proportionally such that the block is skewed back into a square shape. The contour of the modified surface is shown in Fig. 28. Now the data set is aligned with the designed values and is ready for the analysis of the measurement performance quantitatively. The first three of the preceding four adjustments, rotations about the x-, y-, and z-axis, made to the scanning data are rigid body transformations which do not alter the relative distance between any two points. They are necessary only when absolute comparison between scanning data and model is needed. However, for the fourth adjustment, the data is skewed or shifted proportionally along the x-axis. This is similar to the yawing angle calibration

---

[4]Here, the order of the rotations is commutative because the angles involved are very small.

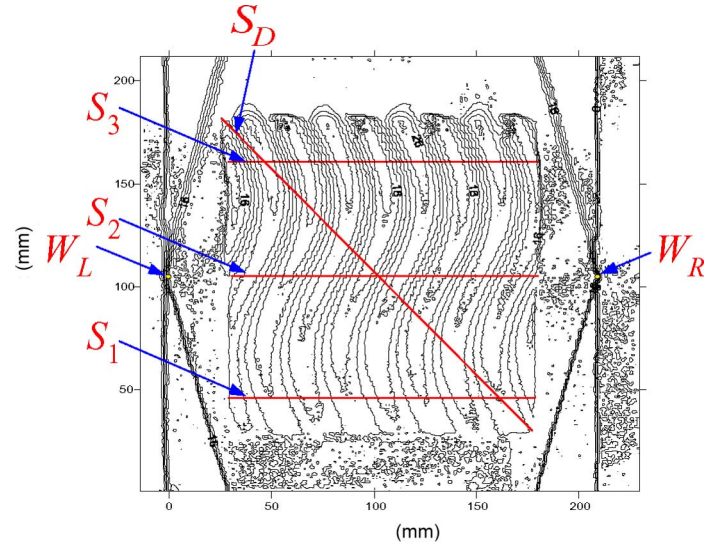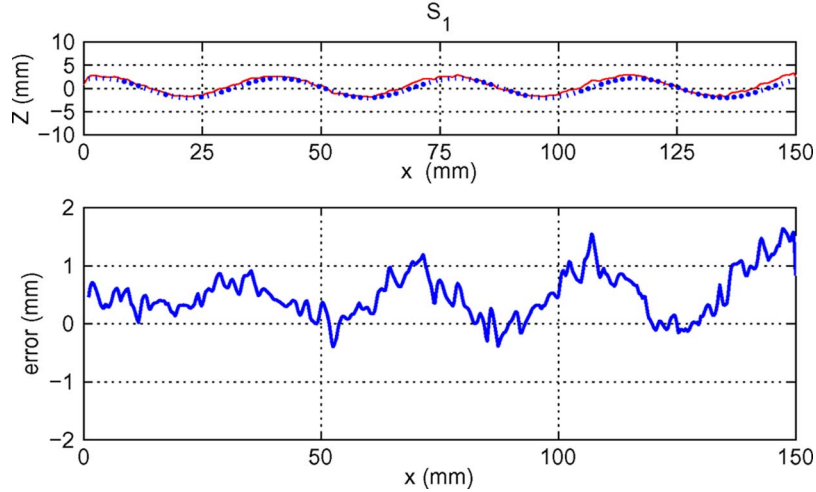Fig. 29. Measurements (solid curves) versus CAD model theoretical values (dotted curves) at S_1 on the CNC machined workpiece of the simulated sandwave.
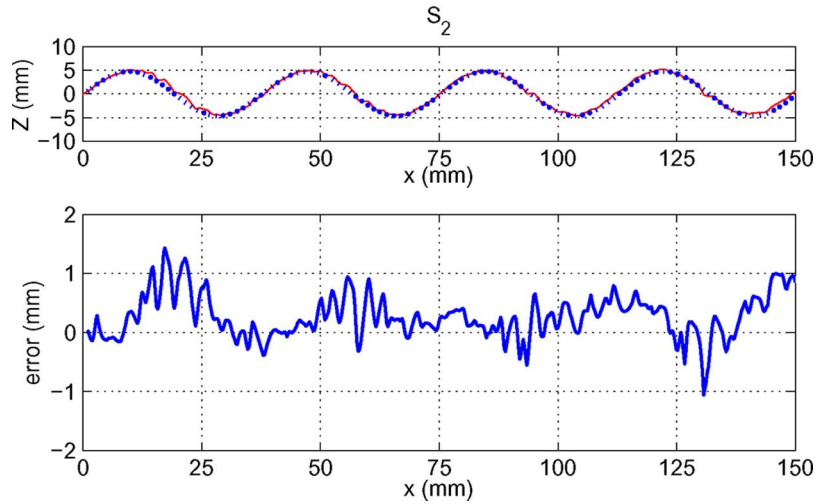

Fig. 30. Measurements (solid curves) versus CAD model theoretical values (dotted curves) at S_2 on the CNC machined workpiece of the simulated sandwave.

for a multibeam echo sounding system. Therefore, this calibration should be done whenever the scanning head is unmounted and remounted back on the track.

We use the interpolated values of the calibrated scanning data at given locations for comparison. Four slices denoted as S_1, S_2, S_3, and S_D in Fig. 28 are selected for analysis. These locations are selected to verify the accuracy of the scanning system in measuring elevation changes of different amplitudes. The amplitude of the sine wave increases from 2 mm for S_1 to 7.5 mm for S_3. S_D is selected to examine the overall accuracy of the scanning and it also indicates whether the phase shift between different ripples is captured correctly. The results are presented in Figs. 29–32. From the results, we find that most of the errors are bounded between −1 and 1.5 mm except for the upper-left segment of the slice S_D. With this spatial resolution and accuracy, conservatively speaking, the laser scanning system should be able to provide interface roughness information needed for modeling acoustic bottom interaction for 100 kHz (wavelength 15 mm) or lower.

The error seems to vary in a fashion similar to the target profile itself. Take slice S_1, for example; the error curve has five

peaks and four valleys. This is also the number of peaks and valleys in the target profile. However, there seems to be a shift between the locations of the features in the target profile and in the error curve. This is an indication that the image processing technique we use to locate the center of the laser stripe is affected by the backscattering pattern of the laser stripe. The measurement results could, therefore, be refined if a functional relationship between the concavity of the feature and the error are found.

V. DISCUSSION

A. Fitting Methods

As we stated in Section II, the effectiveness of the calibration depends on the curve-fitting of the control points. From the measurement results listed in Table I, we found that first-order rms fitting is not as good as second-order rms for most cases. This is because the longitude/latitude lines are not straight in the images. A second-order rms fit provides a better characterization of the control points. Surprisingly, cubic B-spline fitting does not give us satisfactory results in that it does not have a stable error bound. For one case, $\overline{B_2B_3}$, the error is as small as 0.09%; for
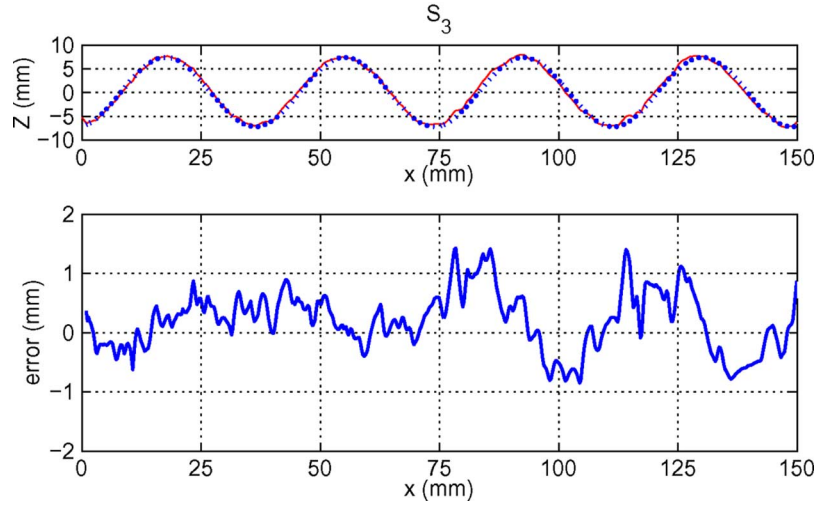
Fig. 31.   Measurements (solid curves) versus CAD model theoretical values (dotted curves) at S_3 on the CNC machined workpiece of the simulated sandwave.
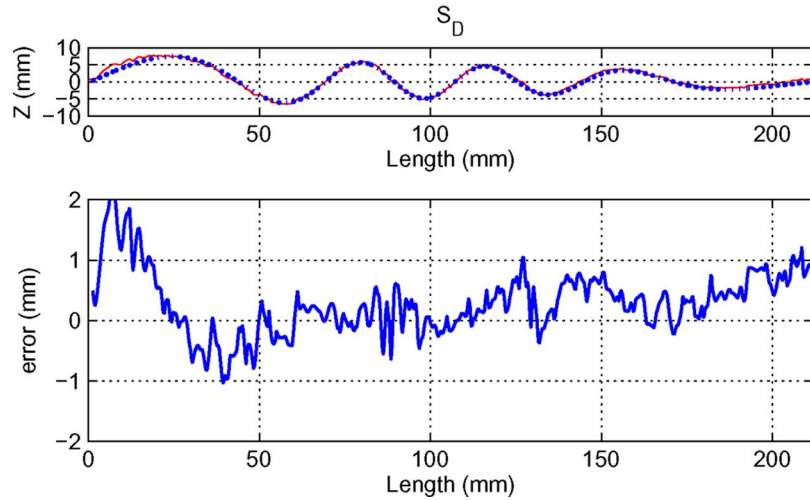

Fig. 32.   Measurements (solid curves) versus CAD model theoretical values (dotted curves) at S_D on the CNC machined workpiece of the simulated sandwave.

the other case, $\overline{A_1 A_2}$, it is as large as 7.28%. The error seems to vary randomly. Because the cubic B-spline fit is forced to pass through all control points smoothly, the fit changes concavity between control points. The change in concavity is very sensitive to the neighboring control points. In Fig. 33, we show fits for two sets of data points with cubic B-spline curves. These two fits share the same data points except that P_2 and P_2' are off by one pixel. We can see that the curves are sensitive to the location of the control points. In shifting P_2 up a pixel, the curvature changes sign between points. As a result, this inevitably introduces errors into the algorithm. On the other hand, if we fit the data points with second-order rms, the curvature of the fit is not so sensitive to the change of one single point, as sees in Fig. 34. This explains why the performance of cubic B-spline for fitting control points is not as good as we may expect.

B. CCD Resolution Versus Subpixel Sampling

The CCD camera used in this paper is an inexpensive ($40), off-the-shelf model for Internet videoconferencing. The CCD screen has 480×640 pixels and its optical quality is much less than that used for professional image processing. We chose this camera deliberately for two reasons: to reduce the cost of the system and to explore the limits of the proposed algorithm. Because of the refraction effect between the viewport glass and the water, the field of view of the camera gets narrower in the water. The camera was placed roughly 1 m from the laser scanning sheet to have a field of view of about 45 cm high and 55 cm wide. This area is covered by the 480×640 pixels. Roughly speaking, each pixel corresponds to about 1 mm along the vertical and horizontal directions. This is the optical limitation for the setup. Actually, even when we replace the camera with a high resolution one, such as 768×1024 pixels, the spatial resolution is still larger than half of a millimeter; so, increasing the resolution of the CCD alone does not improve the spatial resolution of the scanning efficiently. Therefore, to increase resolution below 0.5 mm, subpixel sampling was employed.[5]

[5]For application where the camera is far away from the seabed, increased CCD resolution is the only way to acquire images showing the fine texture.
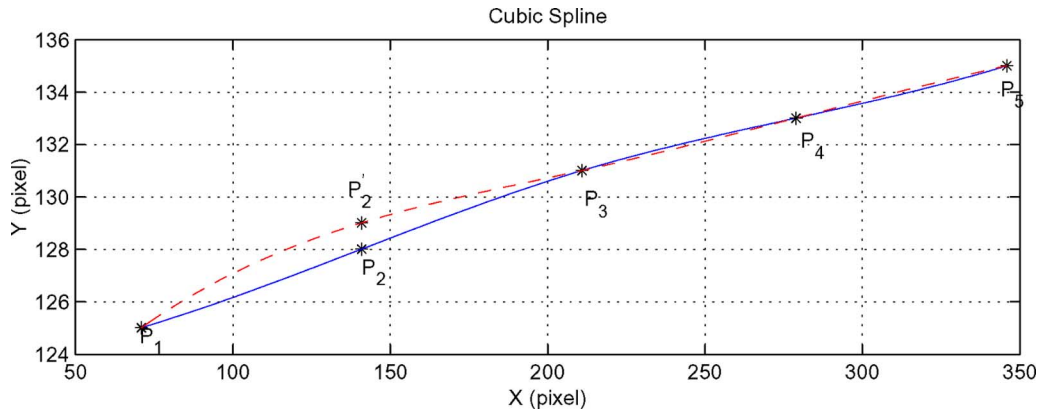
Fig. 33. Trend of curvature changes significantly for cubic B-spline fitting even when only one of the control point is shifted one pixel vertically.
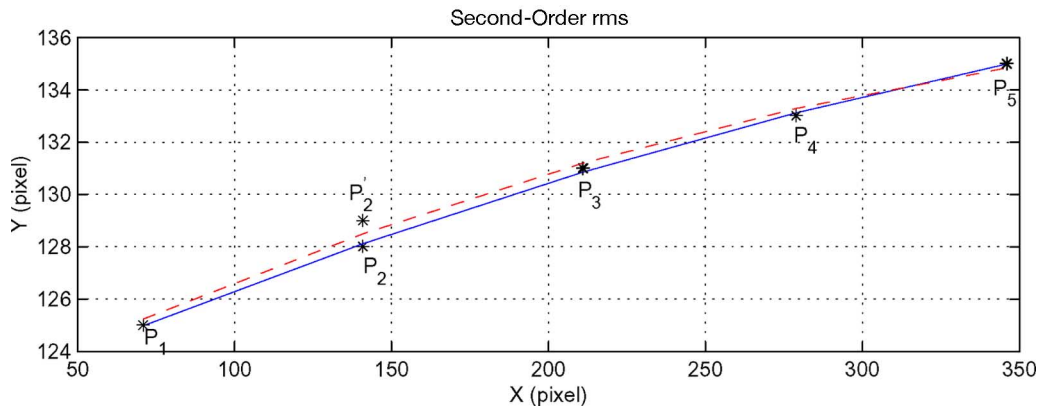

Fig. 34. Change of a second-order rms fit is mild compared with cubic B-spline.
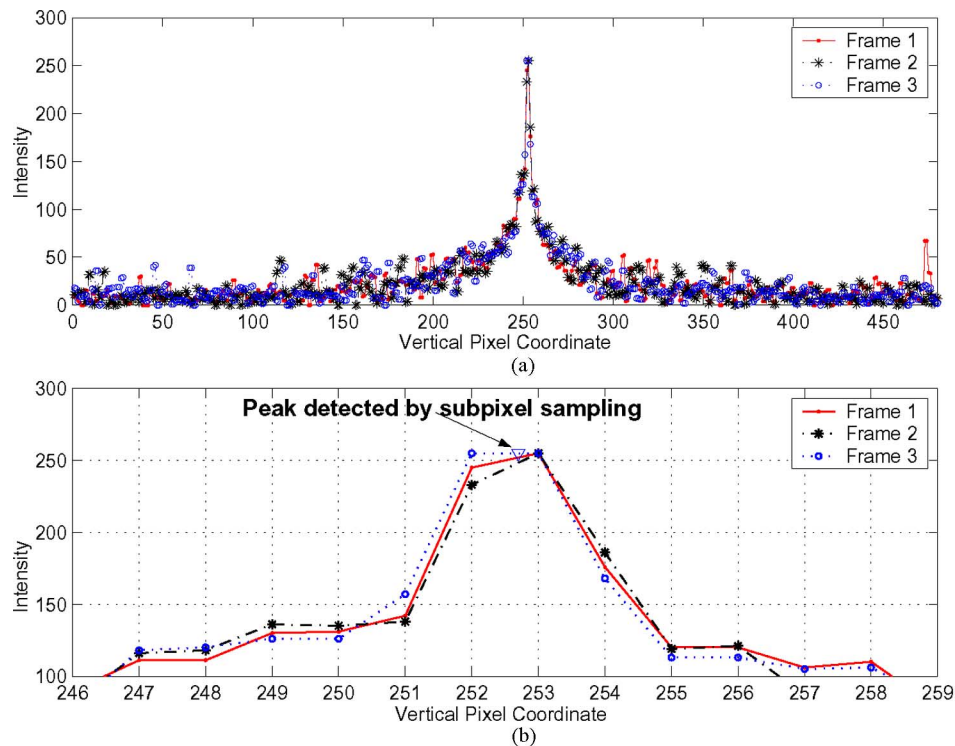

Fig. 35. (a) Pixel intensity variation of the 320th column of the image in Fig. 24 (three consecutive grabbings). (b) Zoom-in of the pixel intensity in the neighborhood of the peak in (a).

Let us look at the intensity contents of a scan. In Fig. 35(a), we plot an intensity curve which corresponds to the 320th column of the image shown in Fig. 24. Only the red component of the intensity is shown because we use a red-diode laser as the pro-

jection light source. Three consecutive frames were grabbed at the same location for comparison. The peaks of the three acquisitions all appear around pixel 250 which corresponds to the location of the laser reflection. A closeup of the peaks is shown in Fig. 35(b). It is obvious that the intensity of pixels 252 and 253 is much higher than the others. For this specific case, these two pixels definitely belong to the laser reflection. What about their neighboring pixels, 251 and 254? Are they within the boundary of the laser reflection? Meanwhile, the intensity also fluctuates slightly from frame to frame. For frame 3, the peak consists of two pixels with roughly the same intensity, while for frames 1 and 2, one pixel's intensity is slightly higher than the other's. Therefore, we cannot just choose the pixel with the largest intensity to represent the center of the reflection because the peak may have multiple pixels with the same intensity or the intensity may vary from frame to frame. A better approach is to estimate the location of the center in continuous pixel coordinate space from the discrete pixel intensity.

One such approach is to calculate the centroid of the bright pixels with intensity as the weighting

$$v_m = \frac{\sum_{i=-s}^{s} I(i)v(i)}{\sum_{i=-s}^{s} I(i)} \tag{8}$$

where $I(i)$ and $v(i)$ are the intensity and vertical coordinate of pixel i, respectively, with $i = 0$ corresponding to the brightest pixel in the column and s defining the span of pixels involved. This is similar to the idea of center of mass. For the case shown in Fig. 35, the vertical coordinate and the intensity $(v(i), I(i))$ of the peak and its two-pixel neighbors are

$$\{(251,142), (252,245), \underline{(253,255)}, (254,176), (255,120)\}_1$$
$$\{(251,138), (252,233), \underline{(253,255)}, (254,186), (255,119)\}_2$$
$$\{(250,126), (251,157), \underline{(252,255)}, (253,255), (254,168)\}_3$$

where the underlined sets correspond to the nominal peaks and the subscripts of the braced brackets denote the frame number. It can be noticed that there are two pixels in frame 3 that have the saturated intensity 255. The algorithm searches the maximum intensity top–down along the column so when there are multiple candidates as the maxima, the pixel with a smallest vertical index will be chosen to represent the nominal peak. Substituting these values into (8), we find the subpixel resolution peaks to be $v_{m_1} = 252.8795$, $v_{m_2} = 252.9087$, and $v_{m_3} = 252.2313$ for frame 1, 2, and 3, respectively. These three subpixel-sampled peaks all lie between 252 and 253. The largest and the smallest values are off by 0.6774 pixel, and the estimated peaks seem to be biased toward the original peak. In other words, the algorithm is sensitive to the choice of the nominal peak. Instead of the original intensity values, let us use the relative intensity as the weighting, so the intensity and pixel data are modified to be

$$\{(251,22), (252,125), \underline{(253,135)}, (254,56), (255,0)\}_1$$
$$\{(251,19), (252,114), \underline{(253,136)}, (254,67), (255,0)\}_2$$
$$\{(250,0), (251,31), \underline{(252,129)}, (253,129), (254,42)\}_3.$$

We recalculate with these new values, and find the subpixel peaks to be $v_{m_1} = 252.6657$, $v_{m_2} = 252.7470$, and $v_{m_3} = 252.6909$ for frame 1, 2, and 3, respectively. This time, the results congregate at the middle of the peaks with much a smaller variation, less than 0.1 pixel. With this method, we successfully refine the resolution of the measurement.

VI. CONCLUSION

In this paper, we present a convenient method for calibrating a nonmetric CCD camera for underwater laser scanning. We let the CCD camera capture the image of a calibration board on which grid points of equal span are laid. Longitude and latitude obtained with curve-fitting of the grid points are used to infer the world coordinates of target points. Because the method only uses a board for implementing the calibration scheme, it is easier than other approaches that need a rigid control frame. Only one image of the calibration board is needed, and it can be done before or after the measurement as long as the scanning head is not disassembled yet. Both on-plane measurement and laser scan line profiling give results with percentage error less than 1%. A simulated sandwave model test piece fabricated with CNC milling machine is scanned in the lab tank. The data points are adjusted to reconstruct the surface of a model sandwave. Because the mathematical equation of the sandwave is known, we compare the numerical results with the theoretical values at specific locations. The experiment shows that our approach can measure sandwave of amplitude as small as 2 mm from 1 m away with error bound less than 1.5 mm.

REFERENCES

[1] A. P. Klimley and S. T. Brown, "Stereophotography for field biologist: Measurement of length and three dimensional positions of free swimming sharks," *Mar. Biol.*, pp. 175–185, 1983.

[2] J. D. Broadwater, "Supporting underwater archeology with ocean technology," in *Proc. OCEANS '88*, 1988, pp. 837–839.

[3] S. T. Barnard and M. A. Fischler, "Computational stereo," *Comput. Surv.*, vol. 14, no. 4, pp. 553–572, 1982.

[4] P. R. Wolf, *Elements of Photogrammetry*. New York: McGraw-Hill, 1983, pp. 141–157.

[5] F. H. Moffitt and E. M. Mikhail, *Photogrammetry*. New York: Harper & Row, 1980, pp. 110–132.

[6] R. Y. Tsai, "A versatile camera calibration technique for high-accuracy 3D machine vision metrology using off-the-shelf TV cameras and lenses," *IEEE J. Robot. Autom.*, vol. 3, no. 4, pp. 323–344, Aug. 1987.

[7] R. Li, H. Li, W. Zou, R. G. Smith, and T. A. Curran, "Quantitative photogrammetric analysis of digital underwater video imagery," *IEEE J. Ocean. Eng.*, vol. 22, no. 2, pp. 364–375, Apr. 1997.

[8] E. S. Harvey and M. R. Shortis, "Calibration stability of an underwater stereo viedeo system: Implications for measurement accuracy and precision," *Mar. Technol. Soc. J.*, vol. 32, no. 2, pp. 3–17, 1998.

[9] W. Myers, "Industry begins to use visual pattern recognition," *Computer*, vol. 13, no. 5, pp. 21–31, 1980.

[10] L. Rocher and A. Keissling, "Methods for analyzing three-dimensional scenes," in *Proc. 4th Int. Joint Conf. Artif. Intell.*, 1975, pp. 669–673.

[11] R. C. Gonzalez, K. S. Fu, and C. S. G. Lee, *Robotics: Control, Sensing, Vision and Intelligence*. New York: McGraw-Hill, 1987, pp. 304–309.

[12] Y. Li, T. Y. Young, and C. C. Huang, "Noncontact measurement using line-scan cameras: Analysis of positioning error," *IEEE Trans. Ind. Electron.*, vol. 36, no. 4, pp. 545–551, Nov. 1989.

[13] D. M. Kocak, F. M. Caimi, P. S. Das, and J. A. Karson, "A 3-D laser line scanner for outcrop scale studies of seafloor features," in *Proc. MTS/IEEE Oceans '99*, 1999, vol. 3, pp. 1105–1114.

[14] Y. Ogawa, "Image processing for wet welding in turbid condition," in *Proc. Int. Symp. Underwater Technol.*, Tokyo, Japan, 2000, pp. 457–462.

[15] A. M. Crawford and A. E. Hay, "A simple system for laser-illuminated video imaging of sediment suspension and bed topography," *IEEE J. Ocean. Eng.*, vol. 23, no. 1, pp. 12–19, Jan. 1998.

[16] C. H. Chen and A. C. Kak, "Modeling and calibration of a structured light scanner for 3-D robot vision," in *Proc. Int. Conf. Robot. Autom.*, 1989, vol. 4, pp. 807–815.

[17] D. N. Gujarati, *Basic Econometrics*. New York: McGraw-Hill, 2003, pp. 194–195.

[18] J. D. Leatherdale and J. Turner, "Underwater photogrammetry in the North Sea," *Photogrammetric Record*, vol. 11, no. 62, pp. 151–167, 1987.

[19] P. Saint-Marc, J. L. Jezouin, and G. Medioni, "A versatile PC-based range finding system," *IEEE Trans. Robot. Autom.*, vol. 7, no. 2, pp. 250–256, Apr. 1991.
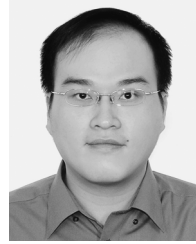
Min-Shine Cheng received the B.S. degree in electronic engineering from I-Shou University, Kao-Hsiung, Taiwan, in 2001 and the M.S. degree in undersea technology from the Institute of Undersea Technology, National Sun Yat-sen University, Kao-Hsiung, Taiwan, in 2004, with a thesis on the development of underwater laser scanning system.

Currently, he is a Manufacturing Engineer in ProMOS Technologies, Hsinchu, Taiwan.
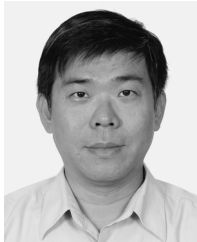
Chau-Chang Wang (M'00) received the B.S. degree from National Taiwan University, Taipei, Taiwan, in 1986 and the M.S. and Ph.D. degrees from University of Pennsylvania, Philadelphia, in 1991 and 1995, respectively, all in mechanical engineering. His dissertation was entitled "Local and Repeatable Coordination Schemes for Redundant Manipulators."

He worked as a Postdoctoral Fellow in the Department of Mechanical Engineering, National Cheng-Kung University, Tainan, Taiwan, for one year. Since 1996, he has been an Associate Professor in the Institute of Undersea Technology, National Sun Yat-sen University, Kao-Hsiung, Taiwan. Further research interests include multibeam echo sounding system data analysis and development of low-power underwater mechatronic systems and underwater robotic systems.